Cubosomal lipid formulation of nitroalkene fatty acids: Preparation, stability and biological effects

Martina Zatloukalová [a], Lukáš Jedinák [b], Daniel Riman [a], Jana Franková [a], David Novák [a], Adrianna Cytryniak [c], Ewa Nazaruk [c], Renata Bilewicz [c], Jiří Vrba [a], Barbora Papoušková [d], Martin Kabeláč [e], Jan Vacek [a,f,*]

[a] *Department of Medical Chemistry and Biochemistry, Faculty of Medicine and Dentistry, Palacký University, Hněvotínská 3, 775 15, Olomouc, Czech Republic*
[b] *Department of Organic Chemistry, Faculty of Science, Palacký University, 17. listopadu 12, 771 46, Olomouc, Czech Republic*
[c] *Faculty of Chemistry, University of Warsaw, Pasteura 1, 02-093, Warsaw, Poland*
[d] *Department of Analytical Chemistry, Faculty of Science, Palacký University, 17. listopadu 12, 77146, Olomouc, Czech Republic*
[e] *Department of Chemistry, Faculty of Science, University of South Bohemia, Branišovská 31, České Budějovice, 370 05, Czech Republic*
[f] *The Czech Academy of Sciences, Institute of Biophysics, Kralovopolská 135, Brno, 612 65, Czech Republic*

ABSTRACT

Lipid nitroalkenes – nitro-fatty acids (NO$_2$–FAs) are formed *in vivo* via the interaction of reactive nitrogen species with unsaturated fatty acids. The resulting electrophilic NO$_2$–FAs play an important role in redox homeostasis and cellular stress response. This study investigated the physicochemical properties and reactivity of two NO$_2$–FAs: 9/10-nitrooleic acid (**1**) and its newly prepared 1-monoacyl ester, (*E*)-2,3-hydroxypropyl 9/10-nitro-octadec-9-enoate (**2**), both synthesized by a direct radical nitration approach. Compounds **1** and **2** were investigated in an aqueous medium and after incorporation into lipid nanoparticles prepared from 1-monoolein, cubosomes **1**@CUB and **2**@CUB. Using an electrochemical analysis and LC-MS, free **1** and **2** were found to be unstable under acidic conditions, and their degradation occurred in an aqueous environment within a few minutes or hours. This degradation was associated with the production of the NO radical, as confirmed by fluorescence assay. In contrast, preparations **1**@CUB and **2**@CUB exhibited a significant increase in the stability of the loaded **1** and **2** up to several days to weeks. In addition to experimental data, density functional theory-based calculation results on the electronic structure and structural variability (open and closed configuration) of **1** and **2** were obtained. Finally, experiments with a human HaCaT keratinocyte cell line demonstrated the ability of **1**@CUB and **2**@CUB to penetrate through the cytoplasmic membrane and modulate cellular pathways, which was exemplified by the Keap1 protein level monitoring. Free **1** and **2** and the cubosomes prepared from them showed cytotoxic effect on HaCaT cells with IC$_{50}$ values ranging from 1 to 8 μM after 24 h. The further development of cubosomal preparations with embedded electrophilic NO$_2$–FAs may not only contribute to the field of fundamental research, but also to their application using an optimized lipid delivery vehicle.

1. Introduction

Nitroalkene fatty acids (NO$_2$–FAs) are endogenous electrophiles produced *via* the interaction of reactive nitrogen species with unsaturated fatty acids. NO$_2$–FAs function as pleiotropic mediators in the signaling adaptive/stress response of the cell [1], regulating redox homeostasis through their interactions with the Keap1-Nrf2 (Kelch-like ECH-associated protein 1- nuclear factor erythroid 2–related factor 2)

[2] and nuclear factor-κB (NF-κB) pathways [3], and selected redox-active enzymes and receptors [4–6]. The main representative of NO$_2$–FAs is nitro-oleic acid (NO$_2$–OA), which occurs in the form of two positional isomers: C9 and C10. The positional isomer C10 and its analogues have been considered as potential drug candidates, because of their cytoprotective, anti-inflammatory and anti-fibrotic activities [7].

The formation of NO$_2$–FAs is based on the nitration of the double bond of unsaturated fatty acids (FAs), see Scheme 1A. There are two mechanisms for the formation of NO$_2$–FAs depending on the presence of

---

List of abbreviations:

ACN	acetonitrile
ACV	alternating-current voltammetry
CE	collision energy
CMC	critical micelle concentration
CPS(A)	constant-current chronopotentiometric stripping (analysis)
CUB	cubosome(s)
CV	cyclic voltammetry
DAF-2	4,5-diaminofluorescein
DAF-2T	4,5-diaminofluorescein triazole
DCC	N,N'-dicyclohexylcarbodiimide
DCM	dichloromethane
DFT	density functional theory
DLS	dynamic light scattering
DMAP	N,N'-dimethylaminopyridine
DMEM	Dulbecco's modified Eagle's medium
DMSO	dimethyl sulfoxide
ESI	electrospray ionization
EtOAc	ethyl acetate
FAs	fatty acids
FCS	fetal calf serum
GAPDH (GADPH)	glyceraldehyde 3-phosphate dehydrogenase
GSH	reduced glutathione
HaCaT cells	human epidermal keratinocyte cell line
HMDE	hanging mercury drop electrode
HOMO	highest occupied molecular orbital
HSA	human serum albumin
ICP-MS	inductively coupled plasma mass spectrometry
Keap1-Nrf2	Kelch-like ECH-associated protein 1- nuclear factor

	erythroid 2–related factor 2
LC	liquid chromatography
LCP	lipidic cubic phase
LUMO	lowest unoccupied molecular orbital
MAG	1-monoolein
MRM	multiple reaction monitoring
MS	mass spectrometry
MTT	3-(4,5-dimethylthiazol-2-yl)-2,5-diphenyltetrazolium bromid
NF-κB	nuclear factor-κB
NMR	nuclear magnetic resonance
NO_2–cLA	conjugated nitro-linoleic acid
NO_2–FAs	nitro-fatty acids
NO_2–LA	nitro-linoleic acid
NO_2–OA	nitro-oleic acid
PAPA NONOate	(Z)-1-[N-(3-aminopropyl)-N-(n-propyl)amino] diazen-1-ium-1,2-diolate
PBS	phosphate-buffered saline
PCM	polarizable continuum model
PGE	basal-plane pyrolytic graphite electrode
PhSeBr	phenylselenyl bromide
SAXS	small-angle X-ray scattering
SDS-PAGE	sodium dodecylsulphate-polyacrylamide gel electrophoresis
SFN	sulforaphane
SIR	selected ion recording
TBNO	*tert*-butyl nitrite
TEMPO	(2,2,6,6-tetramethylpiperidin-1-yl)oxyl
THF	tetrahydrofuran
UPLC	ultra-performance liquid chromatography

either a bis-allylic or conjugated configuration of double bonds, and the main nitration agents are nitrogen oxide radicals ($^\bullet$NO, $^\bullet$NO$_2$) [8]. The first mechanism involves the direct addition of $^\bullet$NO$_2$ to the double bond to form an alkyl radical, in which the intermediate undergoes *cis/trans* isomerization to form the final product. This process only occurs in the presence of relatively high $^\bullet$NO$_2$ concentrations. The second mechanism is typical for FAs or lipids containing conjugated double bonds. The initial FA-radical is stabilized by resonance, which decreases the rate of the elimination reaction and favors reactions with $^\bullet$NO$_2$ or $^\bullet$NO. The produced intermediates decompose to form the final nitroalkenes [9].

NO_2–FAs are known to undergo reversible electrophilic Michael addition with cysteine and other nucleophilic amino acid residues, resulting in the post-translational modification of target proteins (Scheme 1B). Cysteine modification was shown to be relevant for the signaling action of NO_2–FAs [10], histidine adduction was confirmed, and lysine and arginine binding cannot be ruled out [11,12]. The
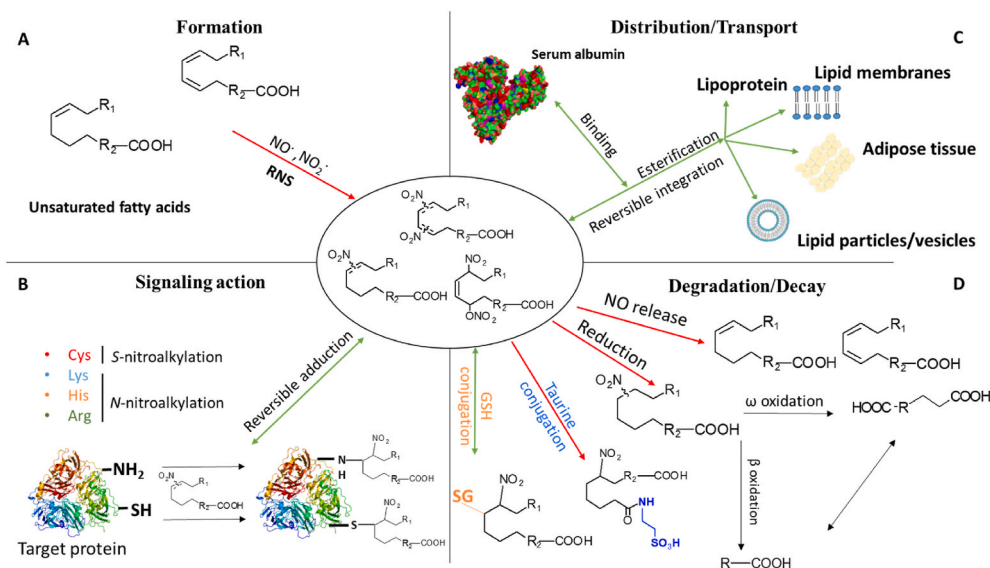
Scheme 1. Overview of the formation, signaling, distribution and degradation pathways for fatty acid nitroalkenes (NO_2–FAs). For more details, see Refs. [56,57] and the *Introduction*. Bis-allylic, conjugated and hybrid NO_2–FAs general structures are shown in the central part.

formation of protein adducts is generally a specific reaction driven by the microenvironment and steric hindrance in the tertiary structure of the proteins. Histidine may exhibit more stable adducts with slower elimination compared to cysteine adducts [13]. Despite the number of pharmacological and biological studies, only a few works have focused on the stability and mechanism of reactivity of NO$_2$–FAs. Recently, we characterized the long-term stability and reactivity of NO$_2$–OA [14], and compared its behavior with nitro-linoleic acid (NO$_2$–LA) and its conjugated form (NO$_2$–cLA) [15].

NO$_2$–FAs undergo a number of metabolic, transport, and degradation processes, which affect or limit their signaling action. In general, NO$_2$–FAs are unstable in water, but they can be stabilized in a lipid environment, polyethylene glycols, alcohols and other less polar organic solvents. The amphiphilic nature of NO$_2$–FAs enables their partitioning and reversible transfer between water and a lipid milieu (Scheme 1C) [8]. In an aqueous environment, they are stabilized by the formation of non-ionic detergent micelles [15] or liposomes [8]. The formation of NO$_2$–FA micelles may affect their reactivity with nucleophiles. The use of octyl glucoside detergent modulated the reaction rate of NO$_2$–OA and NO$_2$–LA with glutathione [16]. In general, there is limited knowledge on the mechanism of the interactions of NO$_2$–FAs with biomembranes. The effect of NO$_2$–FAs on the structure and permeability of membranes and transmembrane proteins was studied by fluorescence measurements and coarse-grained computer simulations [17] and atomistic molecular dynamics simulations [18]. It has been shown that nitrated lipids affect the permeability of cell membranes, forming clusters at the membrane-water interface. The resulting clusters can affect the structural dynamics of selected integral membrane proteins [17].

Protein adduction and esterification into complex lipid structures are considered to be reservoirs of NO$_2$–FAs, which allows their endogenous levels to be regulated [8]. Quantitative LC-MS/MS analysis of radio-labeled 10-nitro-[^{14}C]oleic acid applied *in vivo* showed the accumulation of NO$_2$–FAs in rat adipose tissue. Comparative experiments were performed on adipocyte cell cultures that were incubated with 10-NO$_2$–OA, nitro-stearic acid, NO$_2$–cLA and NO$_2$–LA. It was found that NO$_2$–FAs are preferentially incorporated into monoacyl- and diacylglycerides, while their reduced metabolites are more often transformed into tri-acylglycerides [19]. NO$_2$–FA-protein adducts are reversible in biological systems, and esterified forms of NO$_2$–FAs can be hydrolyzed and mobilized by esterases and lipases, allowing their return to their free active forms [13].

The decomposition of NO$_2$–FAs is associated with the release of the NO radical (Scheme 1D). One of the mechanisms describing the release of the NO radical is based on a modified Neff reaction in a neutral aqueous media. Under these conditions, the formation of the nitronate anion is facilitated, which is subsequently subjected to protonation and deprotonation reactions to form a nitroso intermediate with a weak C–N bond, which leads to $^\bullet$NO release [20]. NO$_2$–FAs can be metabolized by β-oxidation to form shorter products that retain their electrophilic properties, but inactive nitroalkanes without signaling capabilities can also be formed. In addition, NO$_2$–OA is non-covalently bound by serum albumin as an important fatty acid transporter [14] and could be modified covalently by reduced glutathione (GSH) [16]. The binding of NO$_2$–OA to human serum albumin was investigated using electro-chemical and EPR methods. Both methods showed a NO$_2$–OA:HSA binding ratio of 7:1 [14]. The reversibility of GSH-adduction is another possible way that NO$_2$–FAs could be distributed or eliminated *via* the GSH pool [21]. The incorporation of NO$_2$–FAs into lipoproteins is also a way in which NO$_2$–FAs can be distributed systemically.

The aim of this work was (a) to prepare 10-nitro-monoacylglycerol **2**, (b) to compare its reactivity and long-term stability under various experimental conditions with **1** (NO$_2$–OA), (c) to incorporate **1** and **2** into 1-monoolein cubosomes (CUB) as stabilizing lipid nanoparticles. Cubosomes are self-assembled liquid crystalline particles with unique properties that are of practical interest. The most common amphiphilic lipids used to make cubosomes are 1-monoolein and phytantriol.

Hydrating a polar lipid that forms a bicontinuous cubic liquid crystalline phase and then dispersing the phase into stable lipid nanoparticles usually forms cubosomes. Cubosomes have a unique lipidic nano-structure which is biologically compatible and capable of the controlled release of hydrophilic, lipophilic and amphiphilic compounds [22]. Lipidic nanoparticles are also used for the encapsulation of fatty acids. The neuroprotective long-chain omega-3 polyunsaturated fatty acids are poorly water-soluble compounds of low stability upon administration. The encapsulation of the above bioactive lipids into carrier particles such as cubosomes, hexosomes, or spongosomes may provide sustained release, protection and stabilization to avoid eventual aggregation [23]. Other details on cubosomes as nanocarriers for bioactive lipids can be found in a recently reported review [24].

2. Material and methods

2.1. Chemicals

Unless stated otherwise, chemicals were purchased from Merck (Darmstadt, Germany) or BioRad Laboratories (Hercules, CA, USA). Compounds **1** and **2** were synthesized as described in Sec. 2.2. below. The unmodified oleic acid (OA) was purchased from Merck KGaA (Darmstadt, Germany). 1-Monoolein (MAG) was purchased from Hampton Research (Aliso Viejo, CA, USA). All solutions were prepared using Milli-Q water (18.2 MΩ cm^{-1}; Millipore, Bedford, MA, USA). All other used chemicals were of analytical grade.

2.2. Synthesis of nitrated fatty acids and esters

DCM and THF were purified before use by passing them through a column of activated alumina with argon. All other solvents were used at HPLC purity without further purification. *tert*-Butyl nitrite was distilled under reduced pressure before use. All other chemicals were obtained from commercial sources and used as received. Unless otherwise stated, all reactions were carried out in flame-dried glassware under a nitrogen or argon atmosphere. NMR spectra were recorded in a JEOL spectrometer operating at 400 MHz for ^{1}H and 101 MHz for ^{13}C. Samples were dissolved in CDCl$_3$ and measured at 28 °C. Signals were referenced to the residual solvent peak (^{1}H: 7.26 ppm for CHCl$_3$; ^{13}C: 77.16 ppm for CDCl$_3$) and reported in ppm, while coupling constants (J) were reported in hertz (Hz).

2.2.1. Protected glycerol ester of (Z)-oleic acid 5

A three-neck 100 mL round-bottom flask equipped with a magnetic stirrer, thermometer and nitrogen inlet was charged with (Z)-oleic acid **4** (3.63 g, 12.87 mmol), DMAP (0.24 g, 1.93 mmol, 0.15 equiv.), Solketal **3** (2.04 g, 15.45 mmol) and DCM (20 mL). The mixture was cooled in an ice-water bath and a solution of DCC (5.30 g, 25.74 mmol) in DCM (20 mL) was added dropwise over 30 min. After the addition was complete, the mixture was stirred at ambient temperature for 3 days. The mixture was filtered through a pad of Celite, washed with DCM (2 × 20 mL), and evaporated under reduced pressure to yield a colorless oil contaminated with white solid particles. Purification by column chromatography (hexane/EtOAc) yielded the title product as a colorless oil (4.80 g, 94%). ^{1}H NMR (400 MHz, CDCl$_3$): δ = 5.40 – 5.30 (m, 2 H), 4.31 (qd, J = 6.2, 4.8 Hz, 1 H), 4.16 (dd, J = 11.5, 4.7 Hz, 1 H), 4.11 – 4.05 (m, 2 H), 3.73 (dd, J = 8.5, 6.2 Hz, 1 H), 2.34 (t, J = 7.5 Hz, 2 H), 2.05 – 1.98 (m, 4 H), 1.66 – 1.59 (m, 2 H), 1.43 (s, 3 H), 1.37 (s, 3 H), 1.33 – 1.24 (m, 20 H), 0.89 – 0.86 (m, 3 H) ppm. ^{13}C NMR (100 MHz, CDCl$_3$): δ = 173.8, 130.2, 129.9, 110.0, 73.8, 66.5, 64.7, 34.3, 32.1, 29.9, 29.9, 29.7, 29.5, 29.5, 29.3, 29.2, 27.4, 27.3, 26.8, 25.6, 25.0, 22.8, 14.3 ppm.

2.2.2. Protected glycerol ester of (E)-9/10-nitrooleate 6 (method A)

Compound **5** (0.179 g, 0.485 mmol) was added to a 50 mL round-bottom flask equipped with a magnetic stirrer and septa, THF (2.5 mL) and MeCN (2.5 mL) were added *via* syringe through the septa. A

clear colorless solution was cooled in an ice-water bath. After 20 min, $HgCl_2$ (0.158 g, 0.582 mmol) was added in a single portion by temporarily removing the septa. After 10 min, PhSeBr (0.128 g, 0.534 mmol) was added in a single portion by temporarily removing the septa. After 10 min, $NaNO_2$ (0.067 g, 0.970 mmol) was added in a single portion by temporarily removing the septa. The mixture was stirred in an ice-water bath at 0–5 °C for 4 h, and then kept in a freezer (−8 °C) until the next day (16 h).

After 16 h, a pale yellow cloudy solution was passed through Celite and washed with THF (6 × 6 mL). The pale yellow cloudy filtrate was evaporated under reduced pressure at 30 °C to yield a pale yellow oil contaminated with solid particles. This material was treated with THF (2 mL), filtered through cotton and washed with THF (2 × 2 mL). Evaporation under reduced pressure at 30 °C gave a pale yellow oil (0.494 g, without solid particles).

The residue was dissolved in THF (3 mL) to yield a slightly cloudy pale yellow solution. The mixture was cooled in an ice-water bath for 10 min, followed by the dropwise addition of 30% H_2O_2 (1 mL, 9.794 mmol). After 1 h, the mixture was diluted with water (20 mL) and extracted into Et_2O (2 × 20 mL). The combined organic layers were washed with brine, dried over Na_2SO_4 and evaporated. The crude material was purified by column chromatography (silica gel, hexane/EtOAc). A mixture of (*E*)-9/10-nitrooleate **6** was obtained as a colourless oil (0.092 g, 42%). However, (*E*)-9/10-nitrooleate **2** obtained after the hydrolysis of the ketal group was contaminated with a trace amount of Hg (3.4 µg/g of Hg, determined by ICP-MS). Therefore, an alternative mercury-free method for the nitration of lipids was used (see method B).

2.2.3. Protected glycerol ester of (E)-9/10-nitrooleate 6 (method B)

A flame-dried 50 mL round-bottom flask containing a magnetic stirrer was equipped with an efficient reflux condenser opened to the atmosphere through a $CaCl_2$ tube. The reaction vessel was charged with compound **5** (0.396 g, 1.0 mmol), MeCN (4 mL), TEMPO (0.390 g, 2.5 mmol) and *tert*-butyl nitrite (0.297 mL, 2.5 mmol). The mixture was heated in an oil bath to 60 °C for 18 h. Volatiles were removed under reduced pressure, and the residue purified by column chromatography (silica gel, hex/EtOAc). The mixture (*E*)-9/10-nitrooleate **6** was obtained as pale yellow oil (0.174 g), contaminated with an unknown impurity, which was removed after the deprotection step.

2.2.4. Glycerol ester of (E)-9/10-nitrooleate 2

A 25 mL round-bottom flask was charged with (*E*)-9/10-nitrooleate **6** (prepared by method B, 0.174 g) under a nitrogen atmosphere. MeOH (2 mL) was added through the septa, forming a clear solution. 2 N HCl (0.15 mL) was added to this solution. The resulting mixture was stirred at ambient temperature for 3 h. The reaction was then quenched with aqueous $NaHCO_3$ (30 mL), extracted into DCM (2 × 20 mL), dried over $MgSO_4$, filtered, and evaporated under reduced pressure. The crude material was purified by column chromatography (silica gel, hexane/EtOAc). The mixture of isomers (*E*)-9/10-nitrooleate **2** was obtained as a pale yellow oil (0.098 g, 24% over two steps, 23% from oleic acid **4**). ^{1}H NMR (400 MHz, CDCl$_3$): δ = 7.10 – 7.05 (m, 1 H), 4.21 (dd, *J* = 11.6, 4.6 Hz, 1 H), 4.17 – 4.13 (m, 1 H), 3.96 – 3.91 (m, 1 H), 3.70 (dd, *J* = 11.4, 4.1 Hz, 1 H), 3.60 (dd, *J* = 11.5, 4.8 Hz, 1 H), 2.56 (t, *J* = 7.5 Hz, 2 H), 2.37 – 2.33 (m, 2 H), 2.24 – 2.18 (m, 2 H), 1.66 – 1.60 (m, 2 H), 1.53 – 1.44 (m, 4 H), 1.35 – 1.24 (m, 16 H), 0.90 – 0.86 (m, 3 H) ppm. ^{13}C NMR (101 MHz, CDCl$_3$): δ = 174.4, 174.3, 152.1, 151.9, 136.8, 136.4, 70.4, 65.4, 65.4, 63.5, 34.2, 31.9, 29.5, 29.4, 29.4, 29.4, 29.3, 29.3, 29.3, 29.1, 29.1, 29.1, 29.0, 28.7, 28.6, 28.2, 28.1, 28.0, 28.0, 26.5, 26.4, 24.9, 24.9, 22.8, 14.2 ppm.

2.2.5. (E)-9/10-Nitrooleic acid 1

A mixture of (*Z*)-oleic acid **4** (0.355 g, 1.26 mmol), TEMPO (0.29 g, 1.86 mmol) and TBNO (0.30 mL, 2.53 mmol) in MeCN (5 mL) was stirred in a preheated oil bath at 60 °C under a reflux condenser opened to the atmosphere through a $CaCl_2$ tube for 4 days. Volatiles were

removed under reduced pressure, and the residue was treated with hexane/Et_2O 1:1, filtered and evaporated onto silica gel. Purification by column chromatography (silica gel, hexane/Et_2O/AcOH 110:10:0.5 to 110:20:0.5) yielded 121 mg of yellow oil, which required further purification.

The crude product was dissolved in MeOH/water and purified by preparative HPLC using a YMC Actus Pro C18 column, 150 × 20 mm, S-5 µm, 12 nm; flow = 15 mL/min; mobile phase A = MeCN, B = 0.1% TFA in H_2O, with the following gradient: 0 – 8 min (20% → 10% B), 8 –10.5 min (10% B), 10.5 – 11.5 min (10% → 20% B), 11.5 – 13 min (20% B); dual wavelength detector (210 and 256 nm); sample injected in 0.9 mL portions. Product eluted in R_t ≈ 9 min. Combined fractions (∼ 100 mL) containing both 9/10-NO_2 isomers were evaporated under reduced pressure at 30 °C to ∼ 20 mL emulsion, which was separated between cyclohexane (20 mL) and water (20 mL). The organic layer was washed further with one portion of water (20 mL), dried over anhydrous Na_2SO_4, and evaporated under reduced pressure at 30 °C. A regioisomeric mixture of (*E*)-9/10-nitrooleic **1** acid in an ∼ 1:1 ratio was obtained as a colourless oil (58 mg, 14%). ^{1}H NMR (400 MHz, CDCl$_3$): δ = 11.23 (br. s, 1 H), 7.11 – 7.03 (m, 1 H), 2.58 – 2.54 (m, 2 H), 2.37 – 2.32 (m, 2 H), 2.24 – 2.17 (m, 2 H), 1.70 – 1.59 (m, 2 H), 1.54 – 1.44 (m, 4 H), 1.37 – 1.21 (m, 16 H), 0.90 – 0.5 (m, 3 H) ppm. ^{13}C NMR (101 MHz, CDCl$_3$): δ = 179.9, 179.9, 152.2, 151.9, 136.6, 136.3, 34.1, 31.9, 29.5, 29.4, 29.4, 29.4, 29.3, 29.3, 29.3, 29.2, 29.1, 29.0, 29.0, 28.7, 28.6, 28.2, 28.1, 28.1, 28.0, 26.5, 26.5, 24.7, 22.8, 14.2 ppm.

2.3. Critical micelle concentration estimated by DLS

The micelles were prepared by dissolving individual compounds in 1 mM NaOH solution. Each solution was diluted to the final concentration of 100 µM (as sodium salt) with 0.1 M phosphate buffer (pH 7.4). Samples were diluted to several lower concentrations before performing the experiments. Dynamic light scattering (DLS) measurements were performed using a Zetasizer Nano ZSP (Malvern Panalytical, Malvern, UK) at 25 °C. Finally, light scattering intensities (Derived Count Rate, Kcps) were plotted against solute concentration. Critical micellar concentration (CMC) was determined as the intersection between the straight line coming from the light scattering intensity values below the CMC with the straight line derived from the light scattering intensities above the CMC (region of rapid intensity increase). For more details, see Ref. [15].

2.4. DFT calculations

The structure of the OA chain obtained from our previous paper [14] was employed in this study. According to the literature [25] and our findings, there are two most stable conformers of OA and its 9/10-nitro isomers which differ in the torsion angles next to the double bond (close and open ones). The geometry of the studied compound was obtained by the application of a systematic torsion search on the ester part (*R*- stereoisomer was arbitrarily chosen for this study). The structures were further optimized at the DFT level of theory employing the 6–311++G (d, p) basis set and B3LYP functional covering the empirical dispersion term. The software Avogadro was used for the analysis of frontier molecular orbitals and molecular electrostatic potentials (Avogadro: an open-source molecular builder and visualization tool, ver. 1.2.0. http://avogadro.cc). The role of the solvent (water, methanol or *n*-octanol) was treated in an implicit way using the PCM model [26]. All quantum mechanical calculations were performed in the program Gaussian 16 [27].

2.5. Electrochemistry

All electrochemical measurements were carried out at room temperature with a µAutolab III analyzer (EcoChemie, Utrecht, Netherlands) in a three-electrode setup. An Ag|AgCl|3 M KCl electrode

was used as the reference electrode. All potentials were relative to this reference electrode. A glassy carbon rod was used as the auxiliary electrode. A hanging mercury drop electrode (HMDE) was used for constant-current chronopotentiometric stripping (CPS) analysis and alternating-current voltammetry (ACV). Cyclic voltammetry (CV) experiments were measured on a basal-plane pyrolytic graphite electrode (PGE, area 9 mm^2, PG source: Momentive Performance Materials, USA). Individual settings for electrochemical experiments, as well as concentrations of the compounds, are given in the figure legends.

ACV and CV experiments were performed in deaerated 0.1 M phosphate buffer, pH 7.4. All the electrochemical studies were performed *in situ*. The pH measurements were carried out with an HI 2211 pH/ORP Meter (HANNA instruments, Italy).

2.6. Detection of NO release by DAF-2 fluoresce probe

In order to study whether **1** and **2** are able to release an NO radical, the fluorescence probe DAF-2 was used as an NO-trapping agent. Fluorescence intensity was measured in Britton-Robinson buffer (pH 5) at room temperature using a Tecan infinite 200 pro microplate reader. PAPA NONOate was used as a control donor of NO (Cayman Chemical, USA).

2.7. Incorporation of 1 and 2 into lipidic cubic phase (LCP)

LCPs without **1** and **2** were prepared by mixing the appropriate amount of molten 1-monoolein (MAG) and water at room temperature in small glass vials. The ratio of components was chosen on the basis of the phase diagrams for the MAG/water system [28]. The composition of the non-doped LCPs was 60/40 (w/w) % for MAG/water. LCPs with incorporated **1** or **2** were prepared similarly as described above, first samples of **1** or **2** were diluted in MAG solution and mixed with the appropriate amount of water. The final composition of the **1** or **2**-doped LCPs was 55/5/40 (w/w/w) % for MAG/**1**/water and 55/5/40 (w/w/w) % for MAG/**2**/water. Samples were stabilized for at least 24 h to obtain transparent, viscous, and homogenous LCPs. Samples were stored in tightly closed vials at room temperature in the dark. Their stability was confirmed by macroscopic observation of the samples and by small-angle X-ray scattering (SAXS) measurements.

2.7.1. Preparation of cubosomes (CUB)

Cubosomes were prepared by the disintegration of LCP in the presence of 0.5 % Pluronic F-108 in 0.1 M phosphate buffer (pH 7.4) by ultrasonication. The size distribution of cubosomes and corresponding cubosomes with incorporated **1** or **2**, i.e. **1**@CUB and **2**@CUB, were determined by DLS analysis using a Zetasizer Nano ZS (Malvern, UK), see Sec. 2.3. A 45-μL silica cuvette (Hellma, Germany) was used. The measurements were carried out at 25 °C. The size distribution of the cubosomes was expressed as the number distribution of the hydrodynamic diameter.

2.8. SAXS analysis

The phase identity and structural parameters of LCPs were determined by SAXS. The experiments were carried out with a Bruker Nanostar system equipped with a Vantec-2000 area detector using CuKα radiation (λ = 1.54 Å). LCP samples were injected into 1.5-mm diameter quartz capillaries sealed with epoxy glue (UHU). Measurements were performed at 25 °C; scattered intensity was collected over 2 h for dispersed systems and 5 min for bulk LCP. The scattering intensities $I(q)$ were represented as a function of the magnitude of the scattering vector $q = (4\pi/\lambda) \sin(\theta)$, where 2θ is the scattering angle and λ is the wavelength of the incoming X-ray beam. The 2D images were integrated to produce 1D plots representing the scattering intensity I vs. q, called scattering profiles. The lattice parameter (a) for *Pn3m* LCP was calculated using the following equation:

$$a = \frac{2\pi}{q} \sqrt{h^2 + k^2 + l^2}$$

where q is the scattering vector, and h, k, and l are the Miller indices of the Bragg peaks.

To determine the aqueous channel radius, the water volume fraction was estimated using the Eq:

$$\Phi_{water} = \frac{c_{water}}{c_{water} + (1 - c_{water}) \frac{\rho_{water}}{\rho_{lipid}}}$$

where ϕ_{water} is the water volume fraction, c_{water} is the water weight fraction, ρ_{water} is the density of water = 0.997 g ml^{-1}, and ρ_{lipid} is the density of the lipid (ρMAG = 0.942 g ml^{-1}).

Next, the lipid volume fraction was estimated from the Eq.:

$$\phi_{lipid} = 1 - \phi_{water}$$

Lipid length was obtained by solving the Eq:

$$\phi_{lipid} = 2A_0 \left(\frac{l}{a}\right) + \frac{4}{3} \pi \chi \left(\frac{l}{a}\right)^3$$

where l is the lipid chain length/monolayer thickness, a is the lattice parameter of the corresponding phase, A_0 is the Euler–Poincaré characteristic, and χ is the ratio of the area of the minimal surface in a unit cell to (unit cell volume)$^{2/3}$. Finally, the aqueous channel radius was obtained from the Eq.:

$$r_w = \left(-\frac{A_0}{2\pi\chi}\right)^{\frac{1}{2}} a - 1$$

For the *Pn3m* phase, $A_0 = 1.919$, $\chi = -2$, for *Im3m* phase $A_0 = 2.345$ and $\chi = -4$.

2.9. Transmission electron cryomicroscopy

3 μL of cubosome dispersions were applied onto glow-discharged Quantifoil R2/2 holey carbon grids and plunge frozen in liquid ethane using a Vitrobot Mark IV device (Thermo Fisher Scientific). Two-dimensional electron cryomicroscopy images were taken in linear mode on a Thermo Fisher Glacios TEM microscope operating at 200 kV, equipped with a 4k × 4k Falcon 3 EC direct electron detection camera and EPU 2.10 software. The following parameters were used for collecting images: magnification of 92 k, which corresponds to a pixel size of 0.15 nm (1.5 Å) at the specimen level; defocus set to 4.0 μm and 3.5 μm, and the total electron dose of approximately 40 e/Å^2.

2.10. Biological testing

2.10.1. HaCaT cell line

A human keratinocyte cell line (HaCaT) was obtained from CLS (Eppelheim, Germany) and cultivated in DMEM supplemented with FCS (10%), 100 mg/mL penicillin and 100 U/mL streptomycin under standard conditions in a humidified atmosphere (37 °C, 5 % CO$_2$). Each experiment on HaCaT cells was performed three times. The results are expressed as mean ± standard deviation.

2.10.2. Cell viability assay

HaCaT cells on 96-well plates were treated with 0.1% (v/v) DMSO (control), compounds **1** and **2**, **1**@CUB, **2**@CUB, or cubosomes alone or 1.5% (v/v) Triton X-100 (positive control), and the cell viability was determined using MTT reduction assay. This test is based on the ability of the succinic dehydrogenase of living cells to reduce the yellow salt MTT to purple insoluble formazan [29]. Briefly, the cells were washed with PBS and incubated for 2 h at 37 °C with fresh serum-free medium containing 0.5 mg/mL MTT (Sigma). The medium was then removed, and the intracellular formazan produced by active mitochondria was

solubilized in DMSO containing NH_3 (1%, v/v). The absorbance at 540 nm was measured in a spectrophotometric plate reader and used to calculate relative cell viability.

2.10.3. SDS-PAGE and Western blot analysis

Confluent HaCaT cells on 6-well plates were treated for 3 h with serum-free medium containing 0.1% (v/v) DMSO (control), 5 μM sulforaphane (SFN; positive control), 10 μM compounds **1** and **2**, either free or **1**@CUB/**2**@CUB, or cubosomes alone. After treatment, cells were washed with cold PBS, scraped from the plates, pelleted by centrifugation for 3 min at $1500 \times g$ and 4 °C, and lysed in lysis buffer (50 mM Tris, 150 mM NaCl, 1 mM EDTA, 1 mM NaF, 1 mM Na_3VO_4, 1 mM phenylmethylsulfonylfluoride (PMSF), cOmplete protease inhibitors (Roche Diagnostics), 0.2% (w/v) sodiumdodecyl sulfate (SDS), 1% (v/v) Nonidet-P40, 1% (v/v) Triton X-100, pH 7.4). After incubation on ice for 30 min, whole-cell lysates were centrifuged for 10 min at $16\,000 \times g$ and 4 °C, and the supernatants were collected. Proteins in all samples were quantified using a Pierce BCA Protein Assay Kit (Thermo Scientific, Rockford, IL, USA). Aliquots containing an equal amount of protein were subjected to electrophoresis through 4–15% SDS−polyacrylamide gradient gel, proteins were transferred to a polyvinylidene difluoride membrane by electroblotting, and the membranes were probed with primary antibodies, including rabbit monoclonal Keap1 antibody (ab227828; Abcam, Cambridge, MA, USA) and rabbit monoclonal GADPH XP antibody (# 5174; Cell Signaling Technology, Danvers, MA, USA). Primary antibodies were visualized with goat anti-rabbit IgG-HRP secondary antibody (# 7074; Cell Signaling Technology) using a chemiluminescent reaction, and the blots were imaged using a G:Box Chemi-XX6 gel doc system (Syngene, Cambridge, UK). The relative band intensities were evaluated by densitometric analysis using the software ImageJ (National Institutes of Health, Bethesda, MD, USA).

Results were expressed as means. The differences in mean values were analyzed by Student's *t*-test using the software Microsoft Excel (MS office 2016; Microsoft Corporation, Redmond, WA, USA). A *p* value of less than 0.05 was considered to be statistically significant.

2.11. Liquid chromatography/mass spectrometry

The LC method was adopted from Ref. [30]. The experiments were conducted in a Waters ACQUITY UPLC I-Class LC system with a Xevo TQ-S (Waters) triple quadrupole mass spectrometer operating under the control of MassLynx V4.1. The composition of the mobile phase was as follows: 0.1% (v/v) HCOOH in water (solvent A) and 0.1% (v/v) HCOOH in acetonitrile (solvent B). The elution of analytes from an Acquity UPLC BEH C_{18} analytical column (100 mm × 2.1 mm, i.d. 1.7 μm) took place at a flow rate of 0.4 mL/min using the following gradient: 0–10 min 10–95% B, 10–11 min 95% B, 11–13 min 95-10% B followed by 1 min of equilibration. The column temperature was set to 30 °C, and the injection volume was 10 μL.

As for MS parameters, the ESI source operated under the following positive and negative conditions:

ESI^+ (MAG and **2**). The capillary voltage was set to 3.0 kV. The source temperature and the desolvation temperature were set to 150 °C and 320 °C, respectively. The cone and desolvation gas flows were 150 L h^{-1} and 200 L h^{-1}, respectively.

MAG			
MRM transitions	Dwell(secs)	Cone (V)	CE (eV)
1: 357.26 > 265.16	0.080	6.0	10.0
2: 357.26 > 339.27	0.080	6.0	8.0
Compound **2**			
MRM transitions	Dwell(secs)	Cone (V)	CE (eV)
1: 402.25 > 384.28	0.080	38.0	10.0
2: 424.25 > 269.04	0.080	38.0	20.0

ESI^- (OA and **1**). The capillary voltage was set to −2.4 kV. The source temperature and the desolvation temperature were set to 150 °C and 320 °C, respectively. The cone and desolvation gas flows were 150 L h^{-1} and 200 L h^{-1}, respectively.

OA			
SIR transitions	Dwell(secs)	Cone (V)	CE (eV)
1 : 281.16 > 281.16	0.108	80.0	2.0
Compound **1**			
MRM transitions	Dwell(secs)	Cone (V)	CE (eV)
1 : 326.15 > 279.16	0.108	18.0	16.0
2 : 326.15 > 308.19	0.108	18.0	12.0

Compound **2** *m/z* 402.25 $(M + H)^+$, *m/z* 424.25 $(M + Na)^+$, MAG *m/z* 357.26 $(M + H)^+$, compound **1** *m/z* 326.15 $(M − H)^-$, OA *m/z* 281.16 $(M − H)^-$. Bold highlighted transitions were used for calculation and quantification due to better results in terms of S/N ratio.

3. Results and discussion

3.1. Synthesis of nitro-oleic acid (1) and its glycerol ester (2)

The glycerol ester of nitrooleic acid was obtained as an ∼ 1:1 regioisomeric mixture of (*E*)-9- and (*E*)-10-nitrooleate **2**. The synthesis began with the ester coupling of Solketal **3** with (*Z*)-oleic acid **4** using DCC as a coupling agent (Scheme 2) [31]. Nitro functionality was introduced by a standard $HgCl_2$ catalysed nitro-selenation, method A described in Sec. 2.2.2, followed by oxidation using H_2O_2 and spontaneous elimination [32]. However, we sought for an alternative method due to the presence of residual mercury in the final product. The radical nitration of protected ester **5** employing *tert*-butyl nitrite and TEMPO yielded nitrated ester **6**, which upon selective acidic deprotection gave title product **2** in a 23% overall yield [33], see method B in Sec. 2.2.3.

Nitro-oleic acid **1** was previously prepared by a nitro-selenation method from (*E*)-oleic acid **4** [31]. We preferred radical nitration using *tert*-butyl nitrite and TEMPO to avoid issues with removing traces of mercury contamination. In this manner, an ∼ 1:1 regioisomeric mixture of (*E*)-9- and (*E*)-10-nitroleic acid **1** was obtained in a 14% yield (Scheme 3). For NMR data, see Fig. S1 in Supplementary Information.

3.2. Determination of critical micellar concentration by DLS

The critical micellar concentration (CMC) of **1** and **2**, which are only soluble in aqueous media to a limited extent, was determined by DLS method. When present at concentrations above their CMC, **1** and **2** form micelles, vesicles or more complex lipid structures, which is driven by a number of physical and chemical factors such as temperature, pH, CO_2 concentration, presence of detergents or proteins, and others [34].

The CMCs of **1** and other NO_2–FAs have already been reported in our previous work [15]. It is generally known that 1-monooleyl glycerol (1-monoolein, MAG) is practically insoluble in aqueous media [35]. It has been shown that the presence of the NO_2 group in the structure of FAs increases their CMCs, and thus NO_2–FAs become more water soluble compared to the parent FAs [15]. Specifically, the nitration of OA increased the CMC from 2 μM to 10.6 μM. However, the nitration of MAG did not affect its water insolubility, thus compound **2** was practically insoluble in aqueous media, which was confirmed by DLS as described in Sec. 2.3. Knowledge of the CMCs of the studied compounds is one of the crucial parameters for interpreting the reactivity and biological activity of nitrated lipid derivatives. The formation of micelles or other higher lipid structures can isolate the nitro group of NO_2–FAs from an aqueous environment, which could prevent their degradation, but also suppresses their biological activity [8].

3.3. Conformation and electronic structure of 2 by computer simulation

After the esterification, the conformation of alkenyl moiety in **2** remains preserved. Unlike **1**, where both the open and closed structures
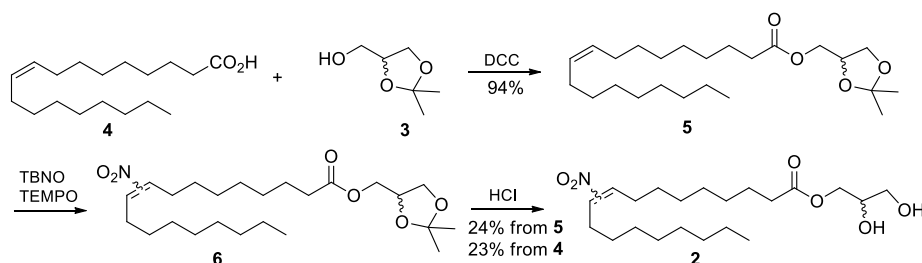
Scheme 2. Synthesis of compound **2**.
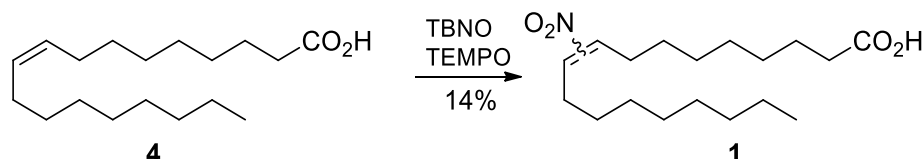
Scheme 3. Synthesis of compound **1**.

have almost the same stability, **2** in the closed conformation is more stable by 17.5 kJ/mol than in the open one due to a favourable interaction of the hydrogens of the ω carbon of **1** part with the oxygens of the glyceryl part. Such interaction also leads to a geometry preference by 1.5 kJ/mol for a closed structure in which the glyceryl part is rotated by 90° with respect to the **1** part over the all *trans* conformation. For the open conformation, the all *trans* conformation of the ester part is preferred.

There is a bigger HOMO-LUMO gap for **2** than for **1**. This is caused by a negative shift of the HOMO by approx. −1 eV, since the HOMO for the ester is located on the C═C bond, whereas for **1** it is situated on the COO⁻ group [14,15]. The character of the LUMO is unchanged – it remains situated on the NO_2 group (*cf.* Fig. 1 and Table 1). A weaker sensitivity of physicochemical properties to choice of solvent was observed for **2** than for **1** due to the lower polarity of **2** [35]. All the above statements are valid both for 9-nitro and 10-nitro isomers. More details on the conformers and electronic structure of **1** can be found in our previous reports [14,15].

3.4. Redox behavior of *1* and *2*

The redox behavior of **1** and **2** was studied at two concentrations of 5 and 50 μM. The concentrations were selected on the basis of previous DLS analyses, *i.e.* below (5 μM) and above (50 μM) the CMC of **1** [15]. The redox properties of **2** were investigated by cyclic voltammetry (CV) at a pyrolytic graphite electrode (Figs. 2A and B). The compounds **4** (OA) and MAG were used as negative controls for which no reduction/oxidation peaks were observed. In our previous work, we dealt with the electrochemical analysis of **1** [14], NO_2-cLA and NO_2-LA [15]. The CV of **1** showed a peak NO at a potential of approx. −0.8 V *vs.* Ag|AgCl|3 M KCl, associated with the reduction of the nitro group (Fig. 2A). The reduction peak NO of **1** was also observed at 50 μM supra-CMC at a similar potential as for 5 μM sub-CMC (Fig. 2B). In addition, we observed a shift of the NO reduction peak of **2** at 5 μM to more negative potentials, indicating that the reduction is suppressed (Fig. 2A).

The final products of the reduction of NO_2–FAs are not yet completely known, the irreversible reduction process (peak NO) most likely leads to the formation of amines, see Ref. [15] and citations
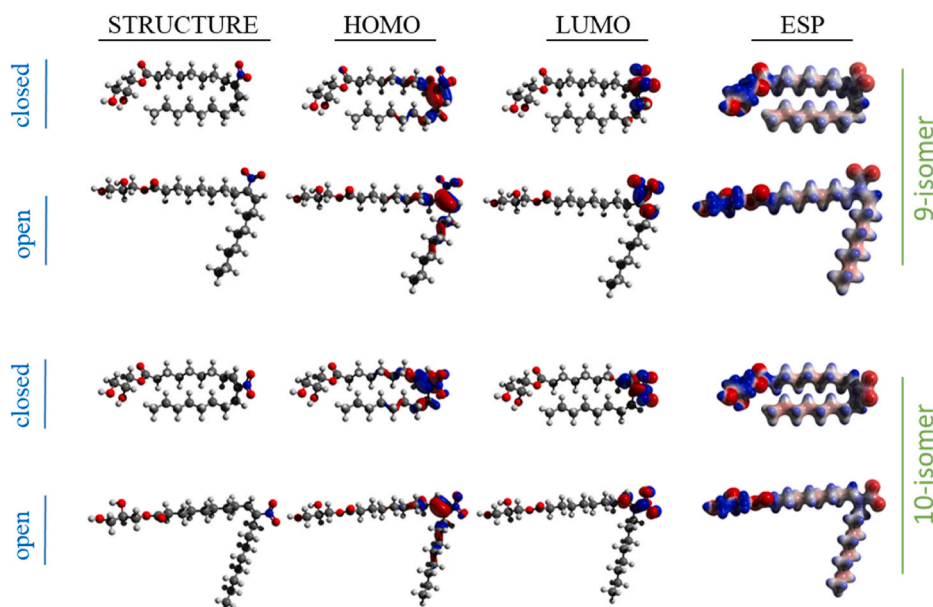

Fig. 1. Molecular (optimized) structure, HOMO, LUMO and ESP-electrostatic potential (from left to right) for closed and open conformers of 9-isomer (upper part) and 10-positional isomer of compound **2**. The structural conformers and electronic structure for **1** can be found in Ref. [15]. ESP: red represents regions with the most negative electrostatic potential, blue represents regions with the most positive one. (For interpretation of the references to color in this figure legend, the reader is referred to the Web version of this article.)

Table 1

Relative energies and HOMO-LUMO characteristics of two most stable conformers of **1** and **2** studied in different solvents. All calculations were performed at B3LYP/ 6–311++G(d, p) level of theory. For the geometry of the conformers, see Fig. 1. Data for **1** were taken from Ref. [15].

	Water				Methanol				n-Octanol			
	ΔE^a	HOMO[b]	LUMO[c]	LUMO-HOMO[d]	ΔE^a	HOMO[b]	LUMO[c]	LUMO-HOMO[d]	ΔE	HOMO[b]	LUMO[c]	LUMO-HOMO[d]
9-isomer	0.00	−9.619	−0.755	8.864	0.00	−9.622	−0.747	8.875	0.00	−9.631	−0.716	8.915
2	17.39	−9.614	−0.790	8.824	17.52	−9.617	−0.780	8.837	17.97	−9.626	−0.746	8.880
10-isomer	0.00	−9.603	−0.760	8.843	0.00	−9.607	−0.752	8.855	0.00	−9.618	−0.722	8.896
2	17.71	−9.587	−0.773	8.814	17.82	−9.589	−0.764	8.825	18.17	−9.597	−0.730	8.867
9-isomer	0.02	−8.286	−0.774	7.512	0.00	−8.188	−0.745	7.443	0.00	−7.808	−0.621	7.187
1	0.02	−8.285	−0.774	7.511	0.02	−8.187	−0.746	7.441	1.08	−7.807	−0.636	7.171
10-isomer	0.00	−8.287	−0.758	7.529	0.00	−8.190	−0.731	7.459	0.00	−7.816	−0.627	7.189
1	1.02	−8.286	−0.771	7.515	1.00	−8.190	−0.744	7.446	0.96	−7.815	−0.640	7.175

[a] relative energy of conformers (in kJ/mol).
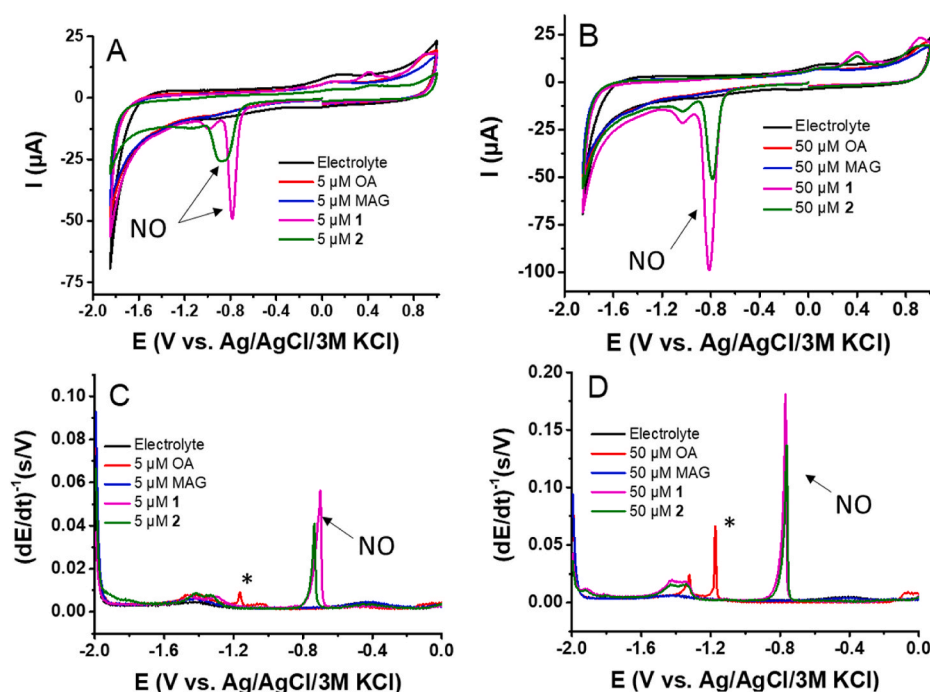[b, c, d] HOMO, LUMO energy and their difference (all in eV).

Fig. 2. Cyclic voltammograms of compounds **1** and **2** and corresponding OA and MAG in Britton-Robinson buffer (pH 7.4) at **(A)** 5 μM and **(B)** 50 μM. CV conditions: initial potential 0 V, first vertex −1.85 V, second vertex 1 V, step potential 5 mV, scan rate 1 V s^{-1}. Chronopotentiometric stripping records of compounds **1** and **2** and corresponding OA and MAG in Britton-Robinson buffer (pH 7.4) at **(C)** 5 μM and **(D)** 50 μM. CPS conditions: accumulation potential 0 V, accumulation time 30 s, potential limit −1.9 V, stripping current −35 μA. (For interpretation of the references to color in this figure legend, the reader is referred to the Web version of this article.)

therein. In the anodic branch of CV records for both **1** and **2**, an oxidation peak at approx. +0.3 V was observed. This oxidation peak was investigated in our previous work, and it was found that the peak is related to the oxidation of the reduction product formed at the electrode surface as a product of nitro moiety reduction proceeding at −0.8 V [15].

The electrochemical behavior of **1** and **2** was also studied using constant-current chronopotentiometric stripping analysis (CPSA) at a hanging mercury drop electrode (Figs. 2C and D). The obtained results were similar to those described by CV. CPSA also showed a second peak (*) at a potential of −1.2 V, which is connected with specific interfacial (adsorption/desorption) behavior (Figs. 2C and D). To better understand the interfacial behavior of **1** and **2**, alternating-current voltammetry (ACV) at the HMDE was performed [14,36]. From the out-of-phase and in-phase AC voltammograms, we can assume that the peak or set of peaks denoted as* are probably due to the adsorption/desorption or reorientation of substances adsorbed at the mercury electrode interface (data not shown). This finding is in agreement with the literature data [14,15,36].

3.5. Stability of 1 and 2 under aqueous condition

The stability over time of **1** and **2** was evaluated by CPSA in buffered media at pH values of 5, 7.4 and 9 in the presence of atmospheric oxygen. The degradation of compounds **1** and **2** was monitored on the basis of the decrease in the NO reduction peak. Under acidic conditions, it was found that both **1** and **2** degraded, which was consistent with previous findings [15] (Figs. 3A and B). At a concentration of 5 μM, the reduction NO peak was not observed after 4 h. At a concentration of 50 μM under identical conditions, the NO reduction signal reached approximately 20 % of the maximum height. This effect is most likely connected with the fact that the compounds are more stable in the micellar state (at 50 μM) than in monomolecular solution.

At the physiological pH of 7.4, there is an increase in the stability of **1** and **2** compared to acidic conditions, and the stability is prolonged in 50 μM samples compared to 5 μM samples. A similar trend was also observed at pH 9 (Figs. 3C–F).

In addition to CPSA, a fluorescence method was used. This approach is based on the conversion of the non-fluorescent probe diamino-fluorescein (DAF-2) to a strong fluorescent triazole (DAF-2T) in the presence of a NO radical [37] (Fig. 4A). NO-release is associated with NO$_2$–FAs decay or degradation under aqueous conditions. The NO
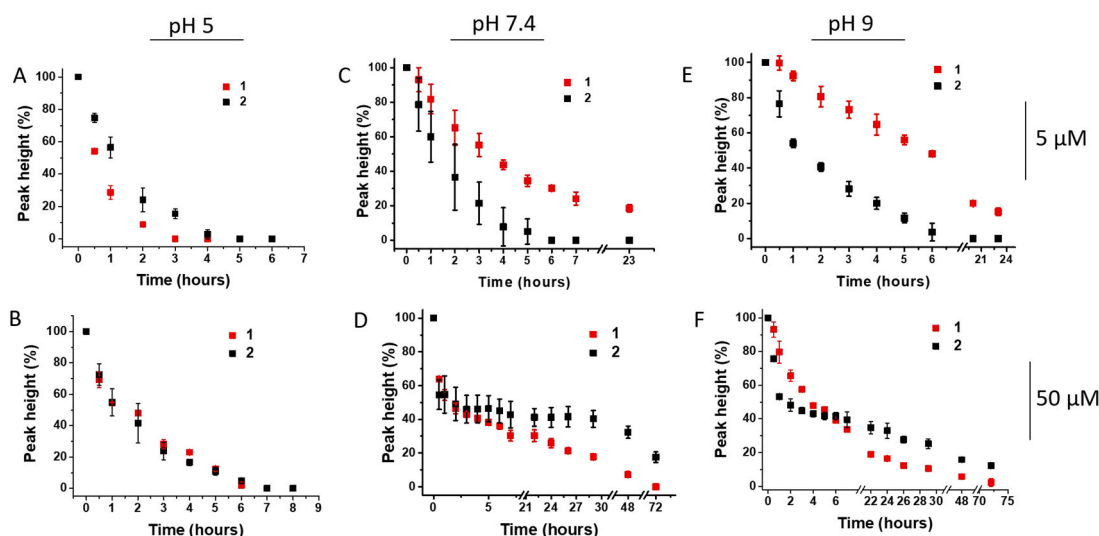
Fig. 3. Stability over time of **1** (red) and **2** (black) represented as NO reduction peak height measured by CPSA at 5 μM (**A, C, E**) and 50 μM (**B, D, F**) in Britton-Robinson buffer at different pH values. CPS conditions: accumulation potential 0 V, accumulation time 30 s, potential limit −1.9 V, stripping current −35 μA. The data are expressed as means ± SD of three independent experiments ($n = 3$). Error bars smaller than the plotted symbols are not visible. (For interpretation of the references to color in this figure legend, the reader is referred to the Web version of this article.)
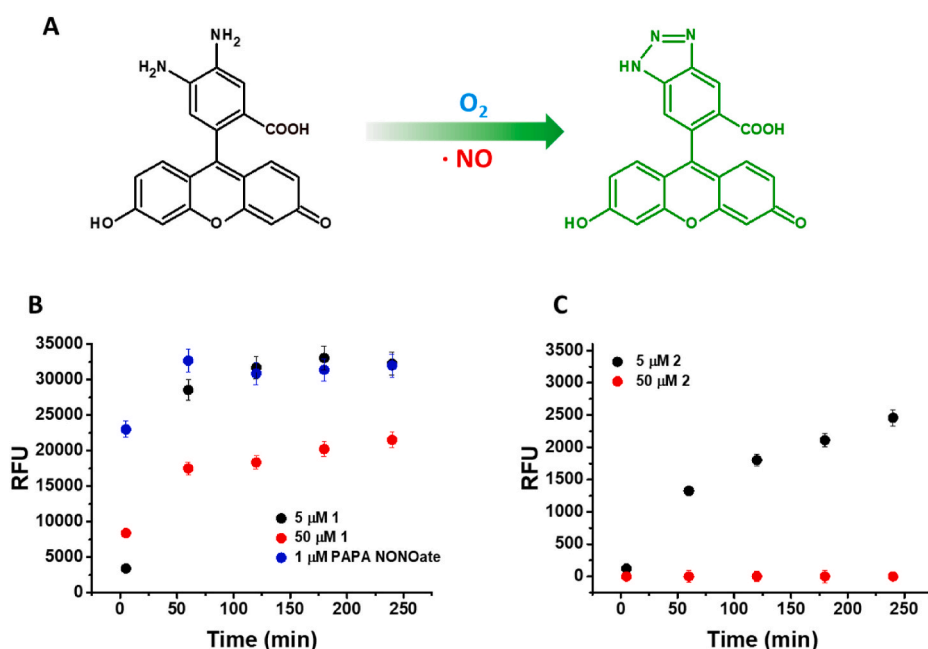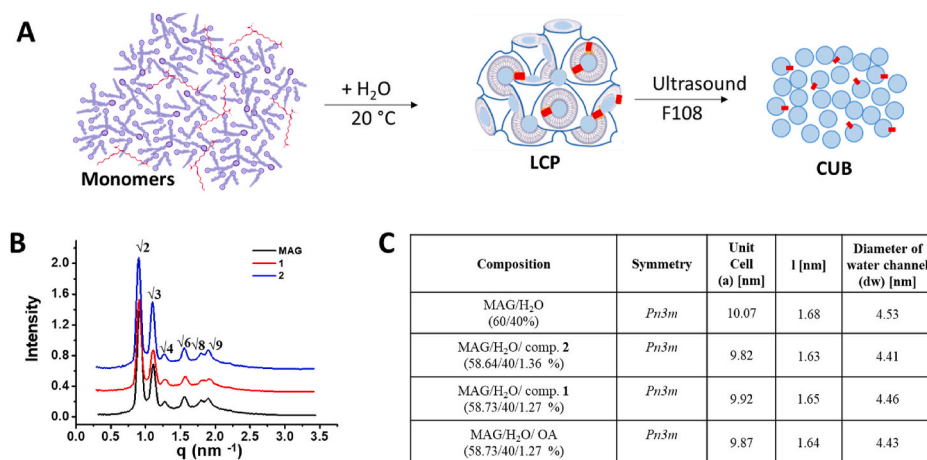

Fig. 4. (A) Transformation of non-fluorescent DAF-2 into fluorescent triazole DAF-2T in the presence of NO radical. Time course of fluorescence at 538 nm corresponding to NO release from compound **1** (panel **B**) and **2** (panel **C**) in Britton-Robinson buffer at pH 5. The data are expressed as means ± SD of three independent experiments ($n = 3$). Error bars smaller than the plotted symbols are not visible. (For interpretation of the references to color in this figure legend, the reader is referred to the Web version of this article.)

donor, PAPA NONOate [38], was used as a positive control in fluorescence experiments. NO radical release was studied in Britton-Robinson buffer (pH 5) at two concentrations of 5 and 50 μM, as in the electrochemical approach above. The fluorescence response of **1** was 10-fold higher than the response of **2** (Figs. 4B and C). Thus, compound **1** releases the NO radical more easily than **2** under the given experimental conditions. The results indicate a stabilization of the nitro group in the micellar and water-insoluble lipid structures, because only 5 μM **1** gives an NO-release kinetic profile similar to the reference compound PAPA NONOate.

3.6. Loading of 1 and 2 into cubosomal lipid nanoparticles

It is generally known that lipid particles can increase the stability and bioavailability of low-molecular lipophilic substances [39–41].

Cubosomes ("smart" lipid nanoparticles [24]) were used as a lipid vehicle for **1** and **2** in this work. Compounds **1** and **2** were incorporated into the lipid cubic phase (LCP) structure as is shown schematically in Fig. 5A. Both compounds were first dissolved in MAG (1-monoolein) and then the formed LCPs were prepared according to the MAG phase diagram as described in Ref. [28]. Many factors can affect the structural parameters of the MAG/water system. The incorporation of various substances such as proteins, detergents and others into the MAG/water system can have a significant effect on the phase behavior [42–44]. The structural parameters of the pure LCP and the LCPs with loaded NO₂–FAs were verified by SAXS analysis (Fig. 5B). For SAXS measurements, pure LCPs with a composition of 60/40 (MAG/water, w/w %) and LCPs with **1** and **2** in a ratio of 55/5/40 resp. 55/5/40 (w/w/w, %) were prepared. The 1D diffraction pattern for the studied LCP exhibited $\sqrt{2}$, $\sqrt{3}$, $\sqrt{4}$, $\sqrt{6}$, $\sqrt{8}$ and $\sqrt{9}$ reflections. These reflections are

Fig. 5. **(A)** Preparation of lipidic cubic phase (LCP) and cubosome preparations **1**@CUB and **2**@CUB. NO_2–FAs and 1-monoolein molecules are highlighted in red and blue, respectively. **(B)** SAXS profiles and **(C)** overview of SAXS parameters: lattice parameters (a), lipid length (l) and aqueous channel diameter (dw) of 1-monoolein (MAG)-based LCP without (black line) or with loaded **1** (red line) and **2** (blue line). (For interpretation of the references to color in this figure legend, the reader is referred to the Web version of this article.)

characteristic of a cubic phase with *Pn3m* symmetry [35]. The symmetry, lattice parameter, lipid chain length and water channel size for LCPs with and without NO_2–FAs are shown in Fig. 5C.

The cubosomes were prepared by the disintegration of LCPs with loaded **1** and **2**, in the presence of 0.5 % polymer Pluronic F-108, using an ultrasound method. The formed cubosomes **1**@CUB and **2**@CUB were stable and consequently characterized by DLS. DLS analysis showed that the prepared cubosomal samples were around 100 nm in diameter (Fig. 6A). Transmission electron cryomicroscopy (Cryo-TEM) was employed to image the obtained cubosome dispersions without changing their structure (Fig. 6). The images revealed a well-ordered internal core of nanoparticles with diameter ranging from around 100 to 200 nm. Cryo-TEM images showed that vesicles are present in cubosomal dispersion which is in accordance with literature [45–47]. The same cubosomal samples **1**@CUB and **2**@CUB were analyzed by using SAXS (Fig. 6B). For the **4** and **1** doped cubosomes the X-ray diffraction measurements show six Bragg peaks with relative positions in ratios $\sqrt{2}:\sqrt{3}:\sqrt{4}:\sqrt{6}:\sqrt{8}:\sqrt{9}$, which are characteristic for the *Pn3m* space group. Lattice parameters for **4**@CUB and **1**@CUB are 9.2 nm and 9.9 nm, respectively. For the cubosomes doped with **2**, the observed scattering peaks can be indexed to coexisting of *Pn3m* and *Im3m* phase

(Fig. 6C). The first set of scattering peaks with $q_{0\ Im3m}= 0.67$ nm^{-1}, have the q positions ratio of $\sqrt{2}:\sqrt{4}:\sqrt{6}$ (marked by stars) which are characteristic for the *Im3m* phase with lattice parameter $a_{Im3m}=13.3$ nm. The second set of scattering peaks starting with $q_{0\ Pn3m} = 0.88$ nm^{-1}, have the reflections at ratios $\sqrt{2}:\sqrt{3}:\sqrt{4}:\sqrt{6}:\sqrt{8}:\sqrt{9}$ characteristic for the *Pn3m* phase with calculated lattice parameter $a_{Pn3m} = 10.1$ nm. For the **2**@CUB the Bonnet ratio a_{Im3m}/a_{Pn3m} is equal to 1.3, this ratio closely matches with that of the Bonnet ratio for coexisting *Im3m* and *Pn3m* phases (the theoretical value a_{Im3m}/a_{Pn3m} is 1.279), see Fig. 6C.

3.7. Stability of **1**@CUB and **2**@CUB

The prepared cubosomes **1**@CUB and **2**@CUB were subjected to CPS analysis at an HMDE in 0.1 M phosphate buffer 7.4 (Fig. 7A). The CPSA showed a reduction in NO peaks of the loaded cubosomes at potentials very close to the peaks of free **1** and **2**, *i.e.* −0.76 V for **1**@CUB, and −0.83 V for **2**@CUB. The CPS responses of pure cubosomes were also observed at around −0.6 V (peak **) and at highly negative potential limits close to hydrogen evolution. The responses are adsorptive in nature (see below) and did not interfere with the NO reduction peaks.
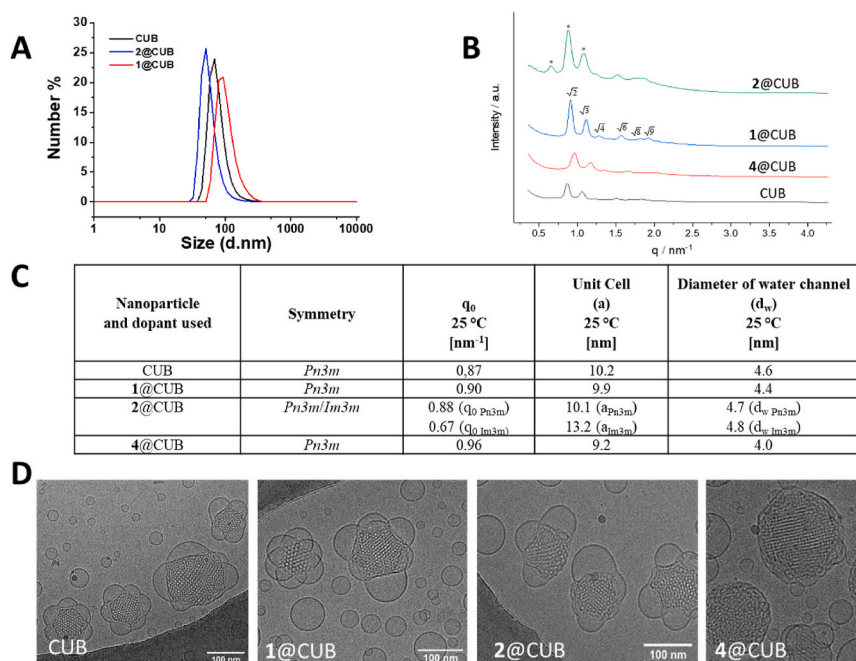

Fig. 6. **(A)** DLS distribution diagrams for pure cubosomes (CUB), **1**@CUB and **2**@CUB. SAXS profiles **(B)** and parameters **(C)** for the cubosomal samples **1**@CUB, **2**@CUB, **4**@CUB (loaded with oleic acid) and pure CUB. **(D)** Two-dimensional electron cryomicroscopy images of pure CUB (left), **1**@CUB, **2**@CUB and **4**@CUB. The final content of compounds **1**, **2** and **4** in CUB samples was 5 % (w/w). (For interpretation of the references to color in this figure legend, the reader is referred to the Web version of this article.)
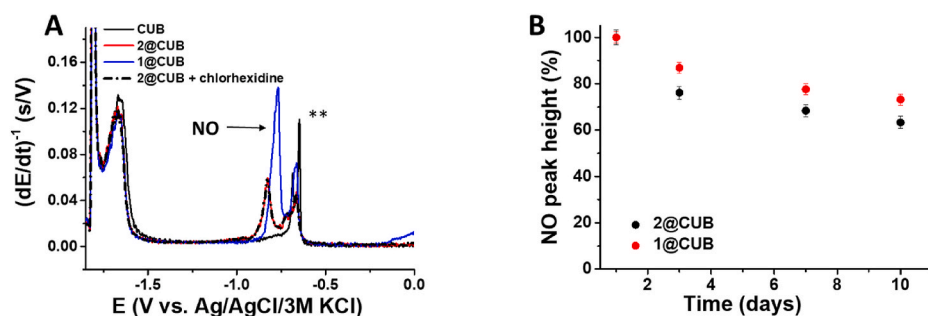
Fig. 7. (**A**) Chronopotentiometric stripping records of 150 μg/mL pure cubosomes (CUB), **1**@CUB, **2**@CUB and **2**@CUB + chlorhexidine in 0.1 M phosphate buffer at pH 7.4. The loaded compound content in CUB was 5 % (w). CPS conditions: accumulation potential 0 V, accumulation time 10 s, potential limit −1.9 V, stripping current −10 μA. (**B**) Long-term stability of **1**@CUB and **2**@CUB measured by CPSA. Chlorhexidine as its acetate salt was 0.1%. The data in panel **B** are expressed as means ± SD of three independent experiments ($n =$ 3). (For interpretation of the references to color in this figure legend, the reader is referred to the Web version of this article.)

The long-term stability was evaluated based on the detection of the NO reduction peak height for **1**@CUB and **2**@CUB (Fig. 7B). A significant prolongation of the stability of both compounds loaded into cubosomes was observed. The reduction NO peak of **1** and **2** in cubosomes reached 70 % of its maximum after 10 days. A degradation/decay of compounds **1** and **2** was documented as a 30% decrease in the NO peak after 24 h. This effect may be associated with **1** and **2** being not properly incorporated into the lipid environment of LCP or their residual presence in aqueous nanochannels. The stability of the NO reduction peak was evaluated for up to 10 days. For a longer time perspective, it is crucial to add a antimicrobial agent to the aqueous phase, *e.g.* chlorhexidine [48], which does not interfere with the CPS detection of NO₂–FAs (Fig. 7A).

The interfacial behavior of pure cubosomes and **1**@CUB and **2**@CUB was studied by ACV at HMDE. In Fig. 8, in-phase and out-of-phase AC voltammograms are shown. In addition to the NO reduction peak and peak ******, a very sharp peak was observed at more negative potentials of hydrogen evolution, most likely due to the very complex adsorption/desorption processes at the surface of the mercury electrode. The evaluation of adsorption/desorption processes was based on the fact that out-of-phase ACV is highly sensitive to adsorption properties in contrast to the in-phase mode; which is sensitive to both diffusion control and adsorption processes as well [14,15,36].

The stability of free **1**/**2** and **1**@CUB/**2**@CUB was further verified by LC-MS analysis (Fig. 9A). For representative LC-MS record, see Fig. S2 in Supporting Information. The test samples were diluted in real culture medium for human HaCaT keratinocytes (see Sec. 3.8) and incubated for 0, 2, 4 and 24 h. Before each analysis, the incubation mixtures were diluted 100-fold with ACN acidified with 0.1% HCOOH, *v/v*. The free **1** and **2** degrade after only 2–4 h, in agreement with the above electrochemical stability evaluation (Fig. 3). The stability of species **1**@CUB and **2**@CUB was 80–90 % based on the LC-MS response evaluation within 24 h of incubation. The free **1** and **2** undergo degradation or elimination reactions, which resulted in approx. 90 % decay after 24 h. The complete dissolution of CUB structures using the acidified ACN procedure was evaluated using DLS (Fig. 9B). After the dissolution of **1**@CUB and **2**@CUB in acidified ACN, approx.100 nm fraction of CUB

was transformed into molecular solution in a fully quantitative manner. DLS analysis was performed 15 min after the **1**@CUB or **2**@CUB dilution in acidified ACN.

3.8. Cytotoxicity evaluation using keratinocyte HaCaT cell line

The cytotoxicity of the free compounds and **1**@CUB and **2**@CUB was tested on the HaCaT cell line using MTT assay [29]. The keratinocyte cell line was selected for our testing, because skin cells are sensitive to NO₂–FAs [49–52] and cubosomes are a prominent delivery vehicle for dermal topical applications [24]. The cytotoxicity of **1** and **2** was first evaluated for 24 h (Figs. 10A and B). Pure cubosomes were found to be non-toxic up to 25 μg/mL, with an IC_{50} value of 67.3 μg/mL (Fig. 10C). This finding is consistent with the reported data on T98G glioblastoma cells, where no cytotoxic effect was observed up to 90 μg/mL [53]. IC_{50} values for both free **1** and **2** and loaded CUB varied from 1 to 8 μM, as shown in Figs. 10D and E.

The uptake of free and CUB-embedded **1** and **2** was investigated by the same LC-MS method as described in the previous section. Our approach was based on the measurement of **1** and **2** depletion in culture media over time, because NO₂–FAs are integrated into more complex lipids intracellularly, and thus their LC-MS analysis cannot be fully quantitative. For uptake experiments, the concentration of compounds applied was 2 μM. No free **1** and **2** were found in culture media after 24 h of incubation with HaCaT cells (Fig. 9A). With **1**@CUB and **2**@CUB, **1** and **2** were analyzed at approx. 10 % of the applied dose in culture media after the 24-h cell cultivation (not shown). After correcting for the degradation factor, calculated based on the results in Fig. 3, the majority of cubosomes (approx. 70 %) were absorbed by the cells or underwent non-specific depletion, *e.g.* surface adsorption.

3.9. Effect of 1 and 2 on the level of Keap1 protein in HaCaT cells

One of the defense systems against oxidative/electrophilic stress in mammalian cells is based, among other things, on the inducible activity of the transcription factor Nrf2, which regulates the expression of many cytoprotective genes. Under unstressed conditions, Nrf2 is negatively
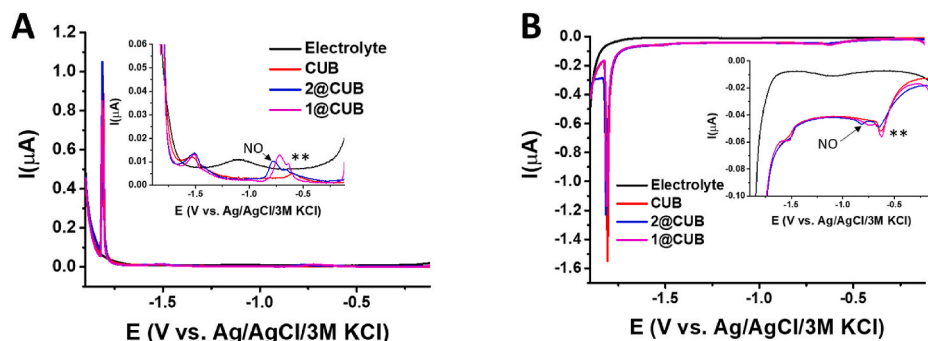

Fig. 8. (**A**) In-phase and (**B**) out-of-phase AC voltammograms of pure 150 μg/mL CUB, **1**@CUB and **2**@CUB. The loaded compound content in CUB was 5 % (w). ACV parameters: initial (0 V) and end (−1.95 V) potentials, frequency: 66.2 Hz, amplitude: 5 mV, phase angle: 0° (in-phase) and 90° (out-of-phase). The electrolytes were degassed for 10 min prior to ACV with argon. (For interpretation of the references to color in this figure legend, the reader is referred to the Web version of this article.)
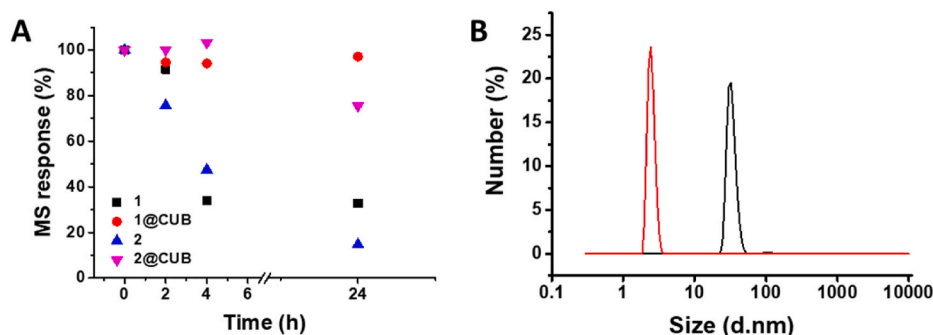

Fig. 9. (A) Stability of free **1/2** and **1@CUB/2@CUB** investigated up to 24 h in HaCaT culture media by LC-MS. Concentration of **1** (24.1 µg/mL), **2** (29.8 µg/mL) and **1@CUB/2@CUB** (100 µg/mL) was used for incubation experiment. Aliquots of incubation mixtures were 100-times diluted with ACN (0.1 % formic acid, *v/v*) prior to LC-MS. **(B)** Size distribution (DLS) of pure 1.2 mg/mL CUB before (black) and immediately (red) after mixing with ACN (0.1 % formic acid, *v/v*). The data in panel **A** are expressed as means $\pm$ SD of three independent experiments ($n = 3$). Error bars smaller than the plotted symbols are not visible. (For interpretation of the references to color in this figure legend, the reader is referred to the Web version of this article.)
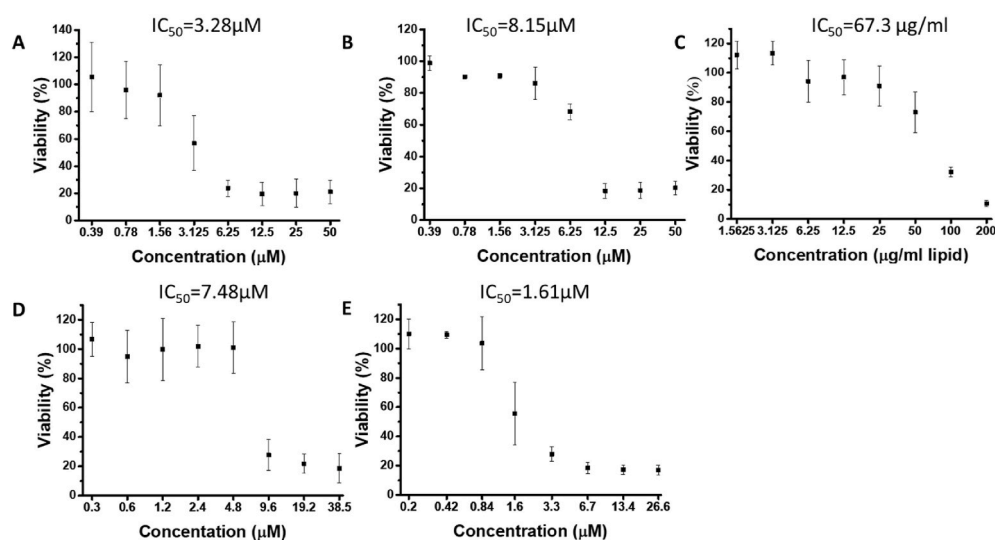

Fig. 10. Cytotoxicity of **(A)** compound **1**, **(B)** compound **2**, **(C)** pure CUB, **(D)** **1@CUB** and **(E)** **2@CUB** in HaCaT cells. The viability was determined by MTT reduction assay after 24 h of exposure. Viability of 100 % = untreated cells. The data are expressed as means $\pm$ SD of three independent experiments ($n = 3$).

regulated through its interaction with Keap1. In contrast, the modification of reactive cysteine residues in Keap1 by oxidants and electrophiles results in the proteasomal and/or autophagic degradation of Keap1 and, in turn, in the activation of Nrf2 [54].

9-NO$_2$–OA was previously shown to downregulate Keap1 in mouse peritoneal macrophages [55]. In this study, we examined using Western blot assay whether **1@CUB** and **2@CUB** affect the protein level of Keap1 in HaCaT cells to confirm that they are biologically active after cell uptake. After 3 h of exposure, we found a weak decrease in Keap1 protein level after the treatment of HaCaT cells with 5 µM sulforaphane, used as a positive control (Fig. 11). A significant decrease ($p < 0.05$) in Keap1 protein was found in cells treated with 10 µM free compound **1** and **1@CUB** compared to untreated (control) cells. In contrast, compound **2** and **2@CUB** did not induce substantial changes, albeit a weak decrease in Keap1 was apparent after normalization to GAPDH. The results also showed that pure cubosomes had no effect on the level of Keap1 in HaCaT cells (Fig. 11). This observation suggested that esterified versions of NO$_2$–FAs will be biologically active to a limited extent.

4. Conclusions

The biological relevance and relationship of NO$_2$–FAs to the development of new drugs is of high interest today [1,7]. NO$_2$–FAs are lipophilic/amphiphilic in nature, and their presence in an aqueous environment may be associated with decay, micellization, and loss of their reactivity [15]. In this study, the modified synthetic protocols for
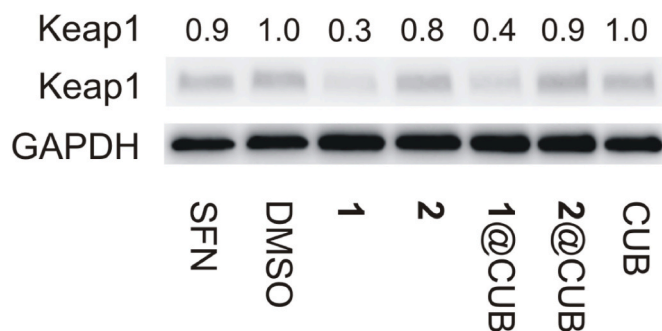

Fig. 11. Effect of compounds **1**, **2** and their cubosomal preparations on Keap1 protein level in HaCaT cells. Cells were treated for 3 h with 0.1% DMSO (control), 5 µM sulforaphane (SFN), 10 µM compounds **1** and **2**, either free or incorporated into cubosomes, or with pure cubosomes (20.1 µg/mL). After treatment, proteins in the whole cell lysates (15 µg/lane) were analyzed by Western blotting, and Keap1 and GADPH were visualized by chemiluminescent detection. Relative Keap1 band intensities normalized to GAPDH are shown. A representative Western blot is shown. Data expressed as folds of the control are means of three independent experiments.

NO$_2$–OA **1** and its ester with glycerol **2** were presented, and both compounds were individually incorporated into cubosomes prepared from 1-monoolein. This is the first application of cubosomes in the research of bioactive electrophiles and RNS. We found that cubosomes enable the

quantitative incorporation of NO$_2$–FAs, and that they represent a suitable vehicle for the physicochemical investigation, long-term stabilization, and biological application/intracellular delivery of NO$_2$–FAs. Using HaCaT keratinocytes, we demonstrated that both cubosomal preparations were absorbed by the cells, where **1** preparations modulated the redox sensor protein Keap1 level. The further development of cubosomal preparations with embedded electrophilic NO$_2$–FAs may contribute not only to the field of fundamental research, but also to their application using an optimized lipid delivery vehicle.

Declaration of competing interest

The authors declare that they have no known competing financial interests or personal relationships that could have appeared to influence the work reported in this paper.

Acknowledgments

Appendix A. Supplementary data

Supplementary data to this article can be found online at https://doi.org/10.1016/j.redox.2021.102097.

References

[1] F.J. Schopfer, N.K.H. Khoo, Nitro-fatty acid logistics: formation, biodistribution, signaling, and pharmacology, Trends Endocrinol. Metabol. 30 (2019) 505–519.

[2] E. Kansanen, H.K. Jyrkkänen, O.L. Volger, H. Leinonen, A.M. Kivelä, S. K. Häkkinen, S.R. Woodcock, F.J. Schopfer, A.J. Horrevoets, S. Ylä-Herttuala, B. A. Freeman, A.L. Levonen, Nrf2-dependent and -independent responses to nitro-fatty acids in human endothelial cells: identification of heat shock response as the major pathway activated by nitro-oleic acid, J. Biol. Chem. 284 (2009) 33233–33241.

[3] T. Cui, F.J. Schopfer, J. Zhang, K. Chen, T. Ichikawa, P.R. Baker, C. Batthyany, B. K. Chacko, X. Feng, R.P. Patel, A. Agarwal, B.A. Freeman, Y.E. Chen, Nitrated fatty acids: endogenous anti-inflammatory signaling mediators, J. Biol. Chem. 281 (2006) 35686–35698.

[4] P.R. Baker, Y. Lin, F.J. Schopfer, S.R. Woodcock, A.L. Groeger, C. Batthyany, S. Sweeney, M.H. Long, K.E. Iles, L.M. Baker, B.P. Branchaud, Y.E. Chen, B. A. Freeman, Fatty acid transduction of nitric oxide signaling: multiple nitrated unsaturated fatty acid derivatives exist in human blood and urine and serve as endogenous peroxisome proliferator-activated receptor ligands, J. Biol. Chem. 280 (2005) 42464–42475.

[5] S. Jobbagy, D.A. Vitturi, S.R. Salvatore, L. Turell, M.F. Pires, E. Kansanen, C. Batthyany, J.R. Lancaster Jr., B.A. Freeman, F.J. Schopfer, Electrophiles modulate glutathione reductase activity via alkylation and upregulation of glutathione biosynthesis, Redox Biol 21 (2019) 101050.

[6] E.E. Kelley, C.I. Batthyany, N.J. Hundley, S.R. Woodcock, G. Bonacci, J.M. Del Rio, F.J. Schopfer, J.R. Lancaster Jr., B.A. Freeman, M.M. Tarpey, Nitro-oleic acid, a novel and irreversible inhibitor of xanthine oxidoreductase, J. Biol. Chem. 283 (2008) 36176–36184.

[7] F.J. Schopfer, D.A. Vitturi, D.K. Jorkasky, B.A. Freeman, Nitro-fatty acids: new drug candidates for chronic inflammatory and fibrotic diseases, Nitric Oxide 79 (2018) 31–37.

[8] B.A. Freeman, P.R. Baker, F.J. Schopfer, S.R. Woodcock, A. Napolitano, M. d'Ischia, Nitro-fatty acid formation and signaling, J. Biol. Chem. 283 (2008) 15515–15519.

[9] G. Bonacci, P.R. Baker, S.R. Salvatore, D. Shores, N.K. Khoo, J.R. Koenitzer, D. A. Vitturi, S.R. Woodcock, F. Golin-Bisello, M.P. Cole, S. Watkins, C. St Croix, C. I. Batthyany, B.A. Freeman, F.J. Schopfer, Conjugated linoleic acid is a preferential substrate for fatty acid nitration, J. Biol. Chem. 287 (2012) 44071–44082.

[10] L. Turell, M. Steglich, B. Alvarez, The chemical foundations of nitroalkene fatty acid signaling through addition reactions with thiols, Nitric Oxide 78 (2018) 161–169.

[11] C. Batthyany, F.J. Schopfer, P.R. Baker, R. Durán, L.M. Baker, Y. Huang, C. Cerveñansky, B.P. Branchaud, B.A. Freeman, Reversible post-translational modification of proteins by nitrated fatty acids in vivo, J. Biol. Chem. 281 (2006) 20450–20463.

[12] L. Turell, D.A. Vitturi, E.L. Coitiño, L. Lebrato, M.N. Möller, C. Sagasti, S. R. Salvatore, S.R. Woodcock, B. Alvarez, F.J. Schopfer, The chemical basis of thiol addition to nitro-conjugated linoleic acid, a protective cell-signaling lipid, J. Biol. Chem. 292 (2017) 1145–1159.

[13] N.K. Khoo, F.J. Schopfer, Nitrated fatty acids: from diet to disease, Curr. Opin. Physiol. 9 (2019) 67–72.

[14] M. Zatloukalova, M. Mojovic, A. Pavicevic, M. Kabelac, B.A. Freeman, M. Pekarova, J. Vacek, Redox properties and human serum albumin binding of nitro-oleic acid, Redox Biol 24 (2019) 101213.

[15] V. Grippo, M. Mojovic, A. Pavicevic, M. Kabelac, F. Hubatka, J. Turanek, M. Zatloukalova, B.A. Freeman, J. Vacek, Electrophilic characteristics and aqueous behavior of fatty acid nitroalkenes, Redox Biol 38 (2021) 101756.

[16] L.M.S. Baker, P.R.S. Baker, F. Golin-Bisello, F.J. Schopfer, M. Fink, S.R. Woodcock, B.P. Branchaud, R. Radi, B.A. Freeman, Nitro-fatty acid reaction with glutathione and cysteine: kinetic analysis of thiol alkylation by a Michael addition reaction, J. Biol. Chem. 282 (2007) 31085–31093.

[17] J. Franz, T. Bereau, S. Pannwitt, V. Anbazhagan, A. Lehr, U. Nubbemeyer, U. Dietz, M. Bonn, T. Weidner, D. Schneider, Nitrated fatty acids modulate the physical properties of model membranes and the structure of transmembrane proteins, Chem. Eur. J. 23 (2017) 9690–9697.

[18] M.C. Oliveira, M. Yusupov, A. Bogaerts, R.M. Cordeiro, How do nitrated lipids affect the properties of phospholipid membranes? Arch. Biochem. Biophys. 695 (2020) 108548.

[19] M. Fazzari, N.K.H. Khoo, S.R. Woodcock, D.K. Jorkasky, L. Li, F.J. Schopfer, B. A. Freeman, Nitro-fatty acid pharmacokinetics in the adipose tissue compartment, J. Lipid Res. 58 (2017) 375–385.

[20] F.J. Schopfer, P.R. Baker, G. Giles, P. Chumley, C. Batthyany, J. Crawford, R. P. Patel, N. Hogg, B.P. Branchaud, J.R. Lancaster, Fatty acid transduction of nitric oxide signaling - nitrolinoleic acid is a hydrophobically stabilized nitric oxide donor, J. Biol. Chem. 280 (2005) 19289–19297.

[21] V. Rudolph, F.J. Schopfer, N.K. Khoo, T.K. Rudolph, M.P. Cole, S.R. Woodcock, G. Bonacci, A.L. Groeger, F. Golin-Bisello, C.-S. Chen, Nitro-fatty acid metabolome: saturation, desaturation, β-oxidation, and protein adduction, J. Biol. Chem. 284 (2009) 1461–1473.

[22] S.A. Gaballa, O.H. El Garhy, H. Abdelkader, Cubosomes: composition, preparation, and drug delivery applications, J. Adv. Biomed. Pharm. Sci. 3 (2020) 1–9.

[23] A. Angelova, M. Drechsler, V.M. Garamus, B. Angelov, Liquid crystalline nanostructures as PEGylated reservoirs of Omega-3 polyunsaturated fatty acids: structural insights toward delivery formulations against neurodegenerative disorders, ACS Omega 3 (2018) 3235–3247.

[24] H.M.G. Barriga, M.N. Holme, M.M. Stevens, Cubosomes: the next generation of smart lipid nanoparticles? Angew. Chem. Int. Ed. 58 (2019) 2958–2978.

[25] S. Mishra, D. Chaturvedi, N. Kumar, P. Tandon, H.W. Siesler, An ab initio and DFT study of structure and vibrational spectra of γ form of oleic acid: comparison to experimental data, Chem. Phys. Lipids 163 (2010) 207–217.

[26] G. Scalmani, M.J. Frisch, Continuous surface charge polarizable continuum models of solvation. I. General formalism, J. Chem. Phys. 132 (2010) 114110.

[27] M.J. Frisch, G.W. Trucks, H.B. Schlegel, G.E. Scuseria, M.A. Robb, J.R. Cheeseman, G. Scalmani, V. Barone, G.A. Petersson, H. Nakatsuji, X. Li, M. Caricato, A.V. Marenich, J. Bloino, B.G. Janesko, R. Gomperts, B. Mennucci, H.P. Hratchian, J.V. Ortiz, A.F. Izmaylov, J.L. Sonnenberg, Williams, F. Ding, F. Lipparini, F. Egidi, J. Goings, B. Peng, A. Petrone, T. Henderson, D. Ranasinghe, V.G. Zakrzewski, J. Gao, N. Rega, G. Zheng, W. Liang, M. Hada, M. Ehara, K. Toyota, R. Fukuda, J. Hasegawa, M. Ishida, T. Nakajima, Y. Honda, O. Kitao, H. Nakai, T. Vreven, K. Throssell, J.A. Montgomery Jr, J.E. Peralta, F. Ogliaro, M.J. Bearpark, J.J. Heyd, E. N. Brothers, K.N. Kudin, V.N. Staroverov, T.A. Keith, R. Kobayashi, J. Normand, K. Raghavachari, A.P. Rendell, J.C. Burant, S.S. Iyengar, J. Tomasi, M. Cossi, J.M. Millam, M. Klene, C. Adamo, R. Cammi, J.W. Ochterski, R.L. Martin, K. Morokuma, O. Farkas, J.B. Foresman, D.J. Fox, Gaussian 16 Rev. C.01, Wallingford, CT.

[28] H. Qiu, M. Caffrey, The phase diagram of the monoolein/water system: metastability and equilibrium aspects, Biomaterials 21 (2000) 223–234.

[29] M.D. Maines, L.G. Costa, D.J. Reed, et al., Current Protocols in Toxicology, John Wiley & Sons, New York, 1998.

[30] C. Mata-Perez, M.N. Padilla, B. Sánchez-Calvo, J.C. Begara-Morales, R. Valderrama, F.J. Corpas, J.B. Barroso, Nitro-fatty acid detection in plants by high-pressure liquid chromatography coupled to triple quadrupole mass spectrometry, Methods Mol. Biol. 1747 (2018) 231–239.

[31] B.E. Coleman, V. Cwynar, D.J. Hart, F. Havas, J.M. Mohan, S. Patterson, S. Ridenour, M. Schmidt, E. Smith, A.J. Wells, Modular approach to the synthesis of unsaturated 1-monoacyl glycerols, Synlett 2004 (2004) 1339–1342.

[32] S.R. Woodcock, G. Bonacci, S.L. Gelhaus, F.J. Schopfer, Nitrated fatty acids: synthesis and measurement, Free Radic. Biol. Med. 59 (2013) 14–26.

[33] S. Maity, T. Naveen, U. Sharma, D. Maiti, Stereoselective nitration of olefins with t BuONO and TEMPO: direct access to nitroolefins under metal-free conditions, Org. Lett. 15 (2013) 3384–3387.

[34] A.L. Fameau, A. Arnould, A. Saint-Jalmes, Responsive self-assemblies based on fatty acids, Curr. Opin. Colloid Interface Sci. 19 (2014) 471–479.

[35] C.V. Kulkarni, W. Wachter, G. Iglesias-Salto, S. Engelskirchen, S. Ahualli, Monoolein: a magic lipid? Phys. Chem. Chem. Phys. 13 (2011) 3004–3021.

[36] L. Havran, S. Billova, E. Palecek, Electroactivity of avidin and streptavidin. Avidin signals at mercury and carbon electrodes respond to biotin binding, Electroanalysis 16 (2004) 1139–1148.

[37] X. Ye, W.-S. Kim, S.S. Rubakhin, J.V. Sweedler, Measurement of nitric oxide by 4,5-diaminofluorescein without interferences, Analyst 129 (2004) 1200–1205.

[38] A.A. Bobko, V.V. Khramtsov, Mechanistic studies of oxidative decomposition of Angeli's salt and PAPA NONOate, Nitric Oxide 40 (2014) 92–98.

[39] M.A. Ali, N. Kataoka, A.-H. Ranneh, Y. Iwao, S. Noguchi, T. Oka, S. Itai, Enhancing the solubility and oral bioavailability of poorly water-soluble drugs using monoolein cubosomes, Chem. Pharm. Bull. 65 (2017) 42–48.

[40] W.K. Fong, R. Negrini, J.J. Vallooran, R. Mezzenga, B.J. Boyd, Responsive self-assembled nanostructured lipid systems for drug delivery and diagnostics, J. Colloid Interface Sci. 484 (2016) 320–339.

[41] A. Angelova, V.M. Garamus, B. Angelov, Z. Tian, Y. Li, A. Zou, Advances in structural design of lipid-based nanoparticle carriers for delivery of macromolecular drugs, phytochemicals and anti-tumor agents, Adv. Colloid Interface Sci. 249 (2017) 331–345.

[42] V. Cherezov, J. Clogston, M.Z. Papiz, M. Caffrey, Room to move: crystallizing membrane proteins in swollen lipidic mesophases, J. Mol. Biol. 357 (2006) 1605–1618.

[43] W. Liu, M. Caffrey, Gramicidin structure and disposition in highly curved membranes, J. Struct. Biol. 150 (2005) 23–40.

[44] Y. Misquitta, M. Caffrey, Detergents destabilize the cubic phase of monoolein: implications for membrane protein crystallization, Biophys. J. 85 (2003) 3084–3096.

[45] D. Demurtas, P. Guichard, I. Martiel, R. Mezzenga, C. Hébert, L. Sagalowicz, Direct visualization of dispersed lipid bicontinuous cubic phases by cryo-electron tomography, Nat. Commun. 6 (2015).

[46] J. Gustafsson, H. Ljusberg-Wahren, M. Almgren, K. Larsson, Submicron particles of reversed lipid phases in water stabilized by a nonionic amphiphilic polymer, Langmuir 13 (1997) 6964–6971.

[47] L. Sagalowicz, M. Michel, M. Adrian, P. Frossard, M. Rouvet, H.J. Watzke, A. Yaghmur, L. De Campo, O. Glatter, M.E. Leser, Crystallography of dispersed liquid crystalline phases studied by cryo-transmission electron microscopy, J. Microsc. 221 (2006) 110–121.

[48] P. Zeng, A. Rao, T.S. Wiedmann, W. Bowles, Solubility properties of chlorhexidine salts, Drug Dev. Ind. Pharm. 35 (2009) 172–176.

[49] A. D'Amore, M. Fazzari, H.B. Jiang, S.K. Luketich, M.E. Luketich, R. Hoff, D. L. Jacobs, X. Gu, S.F. Badylak, B.A. Freeman, W.R. Wagner, Nitro-oleic acid (NO$_2$-OA) release enhances regional angiogenesis in a rat abdominal wall defect model, Tissue Eng. - Part A 24 (2018) 889–904.

[50] A.R. Mathers, C.D. Carey, M.E. Killeen, J.A. Diaz-Perez, S.R. Salvatore, F. J. Schopfer, B.A. Freeman, L.D. Falo, Electrophilic nitro-fatty acids suppress allergic contact dermatitis in mice, Allergy: Eur. J. Allergy Clin. Immunol. 72 (2017) 656–664.

[51] A.R. Mathers, C.D. Carey, M.E. Killeen, S.R. Salvatore, L.K. Ferris, B.A. Freeman, F. J. Schopfer, L.D. Falo, Topical electrophilic nitro-fatty acids potentiate cutaneous inflammation, Free Radic. Biol. Med. 115 (2018) 31–42.

[52] P. Wang, M.E. Killeen, T.L. Sumpter, L.K. Ferris, L.D. Falo, B.A. Freeman, F. J. Schopfer, A.R. Mathers, Electrophilic nitro-fatty acids suppress psoriasiform dermatitis: STAT3 inhibition as a contributory mechanism, Redox Biol 43 (2021) 101987.

[53] E. Nazaruk, A. Majkowska-Pilip, R. Bilewicz, Lipidic cubic-phase nanoparticles—cubosomes for efficient drug delivery to cancer cells, ChemPlusChem 82 (2017) 570–575.

[54] A.T. Dinkova-Kostova, R.V. Kostov, P. Canning, Keap1, the cysteine-based mammalian intracellular sensor for electrophiles and oxidants, Arch. Biochem. Biophys. 617 (2017) 84–93.

[55] R. Saito, T. Suzuki, K. Hiramoto, S. Asami, E. Naganuma, H. Suda, T. Iso, H. Yamamoto, M. Morita, L. Baird, Y. Furusawa, T. Negishi, M. Ichinose, M. Yamamoto, Characterizations of three major cysteine sensors of Keap1 in stress response, Mol. Cell Biol. 36 (2016) 271–284.

[56] G.J. Buchan, G. Bonacci, M. Fazzari, S.R. Salvatore, S.G. Wendell, Nitro-fatty acid formation and metabolism, Nitric Oxide 79 (2018) 38–44.

[57] M. Fazzari, S.R. Woodcock, P. Rowart, K. Ricart, J.R. Lancaster, R.P. Patel, D. A. Vitturi, B.A. Freeman, F.J. Schopfer, Endogenous generation of nitro-fatty acid hybrids having dual nitrate ester (RONO$_2$) and nitroalkene (RNO$_2$) substituents, Redox Biol 41 (2021) 101913.